Article

Multi-Parametric Analysis of Oncology Drug Screening with Aqueous Two-Phase Tumor Spheroids

Pradip S. Thakuri, Stephanie L. Ham, Gary D. Luker, and Hossein Tavana

Mol. Pharmaceutics, **Just Accepted Manuscript** • DOI: 10.1021/acs.molpharmaceut.6b00527 • Publication Date (Web): 21 Sep 2016

Multi-Parametric Analysis of Oncology Drug Screening with Aqueous Two-Phase Tumor Spheroids

Pradip S. Thakuri,[1] Stephanie L. Ham,[1] Gary D. Luker,[2,3,4] Hossein Tavana[1*]

[1] Department of Biomedical Engineering, The University of Akron, Akron, OH 44325 USA

[2-4]Departments of Radiology, Microbiology and Immunology, Biomedical Engineering, University of Michigan, Ann Arbor, MI 48105 USA

*Corresponding author:
Hossein Tavana, Ph.D., P. Eng.
Olson Research Center, Rm 301
260 S. Forge St., Akron, OH 44325
Tel: (330) 972-6031
Fax: (330) 374-8834
E-mail: tavana@uakron.edu

Table of Contents (ToC) Graphic

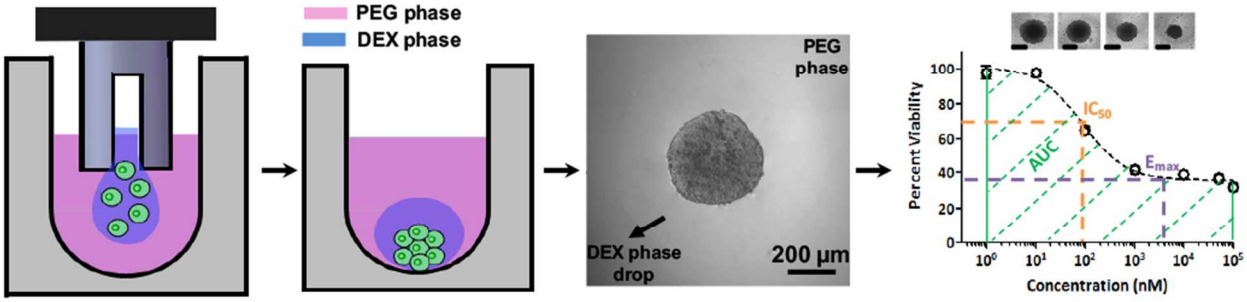

Abstract

Spheroids present a biologically relevant 3D model of avascular tumors and a unique tool for discovery of anti-cancer drugs. Despite being used in research laboratories for several decades, spheroids are not routinely used in the mainstream drug discovery pipeline primarily due to the difficulty of mass-producing uniformly sized spheroids and intense labor involved in handling, drug treatment, and analyzing spheroids. We overcome this barrier using a polymeric aqueous two-phase microtechnology to robotically microprint spheroids of well-defined size in standard 384-microwell plates. We use different cancer cells and show that resulting spheroids grow over time and display characteristic features of solid tumors. We demonstrate the feasibility of robotic, high throughput screening of 25 standard chemotherapeutics and molecular inhibitors against tumor spheroids of three different cancer cell lines. This screening uses over 7,000 spheroids to elicit high quality dose-dependent drug responses from spheroids. To quantitatively compare performance of different drugs, we employ a multi-parametric scoring system using half-maximum inhibitory concentration (IC_{50}), maximum inhibition (E_{max}), and area under the dose-response curve (AUC) to take into account both potency and efficacy parameters. This approach allows us to identify several compounds that effectively inhibit growth of spheroids and compromise cellular viability, and distinguish them from moderately effective and ineffective drugs. Using protein expression analysis, we demonstrate that spheroids generated with the aqueous two-phase microtechnology reliably resolve molecular targets of drug compounds. Incorporating this low-cost and convenient-to-use tumor spheroid technology in pre-clinical drug discovery will make compound screening with realistic tumor models a routine laboratory technique prior to expensive and tedious animal tests to dramatically improve testing throughput and efficiency, and reduce costs of drug discovery.

Keywords: Polymeric aqueous two-phase system, tumor spheroids, robotic, high throughput drug screening, multi-parametric analysis, target validation

Introduction

Cell cultures introduced as a tool for compound screening in 1950s have remained an essential element in the process of oncology drug discovery [1]. In pre-clinical studies, monolayer (2D) cultures of cancer cells are routinely used to assess efficacy of hundreds of candidate drug compounds. However, due to major differences between 2D cultures and three-dimensional (3D) tumor microenvironments of cancer cells *in vivo*, 2D cultures often fail to predict drug activities *in vivo* [2]. This significantly increases attrition rates and costs of anticancer drug development [3]. Despite considerable investments, the rate of introduction of novel drugs has remained relatively constant over the past few decades and only two to three agents in new drug classes make it to the market annually [4–6].

To improve drug discovery outcomes, it is critical to employ cellular models that mimic structural, biological, and functional properties of tumors [7]. Spheroids are 3D compact clusters of cancer cells that model avascular solid tumors, close cell-cell contacts, matrix deposition and cell-matrix interactions, diffusion limitations of oxygen, nutrients, metabolites, and waste products, cell migration from solid tumors,[8] and gene expression profiles of original tumors [9–15]. Despite their clear benefits, spheroids are not routinely used in compound screening applications for anticancer drug discovery. Spheroid culture techniques face difficulties with mass production of consistently-sized spheroids in standard labware, compatibility with robotic instruments for automation of standard drug testing protocols, and ease of culture, maintenance, treatment, and analysis of cellular responses. These difficulties hamper the use of spheroids in mainstream drug development and discovery [16].

To overcome this barrier, we recently developed a tumor spheroid microtechnology based on the use of a polymeric aqueous two-phase system (ATPS) with polyethylene glycol (PEG) and dextran (DEX) as phase-forming polymers [17–19]. Using an optimized robotic liquid handling protocol, a submicroliter drop of the denser aqueous DEX phase containing cancer cells is dispensed into the immersion aqueous PEG phase in each well of standard microwell plates. Due to an ultralow interfacial tension between the aqueous PEG and DEX phases [20], cells remain confined within the drop phase and spontaneously self-assemble into a single, fully viable spheroid [19]. Spheroids within each plate are individually addressable with drug compounds, enabling testing of multiple drugs over a wide concentration range. Unlike several other methods, the use of standard labware and robotics with the ATPS technology significantly simplifies formation, maintenance, drug treatment, and *in situ* optical and biochemical analysis of spheroids.

To establish the feasibility of incorporating the robotic ATPS tumor spheroid microtechnology into drug screening applications, we conduct a comprehensive high throughput screening of 25 different anticancer compounds against tumor spheroids of colorectal cancer, glioblastoma multiforme, and triple negative breast cancer (TNBC) cells. Drug testing, renewal, addition of biochemical analysis reagents, and analysis of cellular responses are done sequentially in the same 384-well plate in which spheroids are formed initially. To show the broad utility of this technology, the collection of compounds is selected to contain both cytotoxic chemotherapeutics and specific molecular inhibitors. In addition to demonstrating the capabilities of robotic drug testing with this microtechnology, we propose to evaluate drug responses of cancer cells in spheroids using two different approaches. First, dose-dependent responses of drug-treated tumor spheroids are analyzed using a multi-parametric approach based on drug efficacy (E_{max}), potency

(IC_{50}), and the area under the dose-response curve (AUC). This approach helps rank all anticancer drugs tested against spheroids of each of the three cancer cells and identify the most effective compounds against each cell type. Second, morphological changes such as growth inhibition and disintegration of spheroids post-drug exposure are used as an independent measure of effectiveness of certain compounds. Finally, we perform a target validation study using protein expression analysis to confirm that phenotypic screening results from testing of specific molecular inhibitors are indeed due to on-target effects of drug compounds. Through this comprehensive set of tests and analyses, we substantiate that the robotic polymeric ATPS approach to 3D culture of cancer cells is uniquely suited for high throughput compound screening and molecular analysis to significantly expedite the discovery of effective anticancer drugs.

Materials and Methods

Cell culture

We used three different lines of cancer cells. MBA-MB-157 breast cancer cells (ATCC), HT-29 colon cancer cells (ATCC), and U-87 MG brain cancer cells (ATCC) were maintained in Dulbecco's Modified Eagle Medium (DMEM), Mc Coy's 5A, and Eagle's Minimum Essential Medium (EMEM), respectively, each supplemented with 10% fetal bovine serum (FBS, Sigma), 1% antibiotic (Life Technologies), and 1% glutamine (Life Technologies). Cells were cultured in a humidified incubator at 37˚C and 5% CO_2. Cells were dissociated using 0.25% trypsin (Life Technologies) from 80-90% confluent monolayer in tissue culture flasks. Trypsin was neutralized using complete growth medium of each cell type. The cell suspension was centrifuged down at 1000 rpm for 5 min. After removing supernatant, cells were suspended in 1 ml of culture medium and counted using a hemocytometer prior to spheroid formation.

Spheroid formation using ATPS

Polyethylene glycol (PEG, Sigma), Mw: 35 kDa, and dextran (DEX, Pharmacosmos), Mw: 500 kDa, were dissolved in the culture medium of each cell type to obtain final stock solution concentrations of 5% (w/v) PEG and 12.8% (w/v) DEX (Figure 1a). A standard 384-well round-bottom ULA plate (Corning), labeled as destination plate, was loaded with 30 µl of the aqueous PEG phase medium. A density of 1×10^5 cells/ml was prepared by suspending cells in culture medium of each cell type. The suspension was thoroughly mixed with an equal volume of the 12.8% (w/v) aqueous DEX phase medium. This reduced DEX concentration to 6.4% (w/v) and adjusted the density of cells to 0.5×10^5 cells/ml. A single column of a flat-bottom 384-well plate (Corning), labeled as source plate, was filled with this cell suspension. Using a robotic liquid handler (Bravo SRT, Agilent), 0.3 µl of cell suspension was aspirated and dispensed into each well of the destination plate containing the aqueous PEG phase. This process was done column-by-column to minimize the required number of cells in the source plate. Prior to each aspiration step, the cell suspension in the source plate was robotically mixed to ensure a uniform mixture. Cells remained confined within the DEX phase drop and formed a single spheroid in each well (Figure 1b). Consistency of spheroid formation was assessed by measuring the diameter of spheroids for each cancer cell line.

Growth kinetics of spheroids

A total of 50 spheroids were imaged daily to assess growth kinetics of spheroids based on their volumes and metabolic activity. Culture medium was renewed every 3 days for a period of 9 days. Phase contrast images of spheroids were captured using an inverted fluorescent microscope (Axio Observer, Zeiss) equipped with a high resolution camera (AxioCam MRm, Zeiss). Diameter of each spheroid was measured using ImageJ, and volume of each spheroid was calculated assuming a spherical shape. Additionally on each day, metabolic activity of cells in spheroids was determined by adding a PrestoBlue reagent (Life Technologies) to wells at 10% of total volume in each well, incubating the plates for 4 hrs, and measuring fluorescence intensity using a plate reader (Synergy H1M, Biotek Instruments) [21].

Immunohistochemical analysis of spheroids

Spheroids were harvested on day 4 of culture, fixed with 3.7% paraformaldehyde, embedded in a freezing medium, and sectioned to 10 µm slices using a cryostat. The largest sections were selected and immunostained for a cell proliferation marker protein Ki-67 (Cell Signaling Technology), and extracellular matrix proteins type I collagen (Abcam), laminin (Sigma), and fibronectin (Sigma). Nuclei were stained with Hoechst (Life Technologies). Fluorescent images were captured using an inverted fluorescence microscope.

Anticancer drug screening against tumor spheroids

We used the following 25 different anticancer compounds: doxorubicin, paclitaxel, 5-fluouracil, ponatinib, oxaliplatin, cisplatin, staurosporine, 17-AAG, critzotinib, ribociclib, KX2-391, VER155008, panobinostat, trametinib, selumetinib, PD0325901, GSK1059615, PI-103, dactolisib, pictilisib, YM155, SP600125, LY2784544, tirapazamine, and hyaluronan-resveratrol (H-R). The first 23 compounds were obtained from Selleckchem and dissolved in DMSO (ATCC) according to the manufacturer's protocols. Stock solutions of these compounds were prepared such that the highest drug concentration used for testing contained less than 0.5% DMSO [22]. At this DMSO concentration, spheroids of cancer cells were viable similar to control spheroids in complete growth media. Tirapazamine was purchased from Sigma and H-R was kindly provided by Dr. Y.H. Yun. Stock solutions of both compounds were prepared in sterile distilled water. Main molecular targets of compounds are listed in Table 1.

With each compound, six different concentrations of 2 nM, 20 nM, 200 nM, 2 µM, 20 µM, and 100 µM were prepared by serially diluting a respective stock solution in culture media of cells. These concentrations were prepared twice the final drug concentrations for testing against tumor spheroids. Next, 30 µl from each of these concentrations for a given drug solution was added to each well of the destination plate that contained a spheroid in the DEX phase drop immersed in 30 µl of the aqueous PEG phase. This addition step diluted concentrations of PEG and DEX, converting the ATPS to a single medium phase containing trace amount of polymers, and reduced drug concentrations to 1 nM, 10 nM, 100 nM, 1 µM, 10 µM, and 50 µM. After 72 hours, 30 µl of each drug at these concentrations was added to the corresponding wells. We have shown that presence of trace concentrations of PEG and DEX does not interfere with drug diffusion through culture media [21]. To minimize evaporation of media and avoid variations in drug concentrations and media osmolality during the testing period, the outermost wells of

the destination plate were filled with sterile water. After 6 days of drug treatment, spheroids were imaged for morphological characterization. Next, PrestoBlue was added to wells and after 4 hrs of incubation, the fluorescence signal was measured with a plate reader. A total of 14 replicates was used for both control (non-treated) and drug-treated spheroids. Viability of spheroids treated with each concentration of a drug was normalized to that of non-treated, control spheroids and expressed as percent viability. GraphPad Prism 5 was used to fit a 4-parameter sigmoidal dose-dependent response curve to the raw viability data and measure IC_{50}, E_{max}, and AUC.

Western blotting

Spheroids were harvested from 384-well plates and transferred into a 50 ml conical tube. After centrifugation and removing of the supernatant, spheroids were washed with PBS, lysed in 500 µL of complete RIPA buffer (50 mM Tris-HCl, 150 mM NaCl, 1% NP-40, 0.5% sodium deoxycholate, and 0.1% SDS, pH 7.4±0.2) with protease inhibitor (complete mini, Roche Diagnostics) and phosphatase inhibitor (Life Technologies). To ensure complete lysis, spheroids were sonicated (Vibra-Cell, Sonics) for 5 seconds twice at a 50% amplitude level. Total protein concentration was determined using a BCA quantification assay kit (Life Technologies). 20 µl of protein was loaded onto a 4-15% gel (Bio-rad) for electrophoresis and the gel was transferred onto a nitrocellulose membrane by electroblotting. Membrane were blocked with 5% BSA (Sigma) for 1 hr. Primary antibodies used were phospho-p44/42 MAPK (Erk1/2), p44/42 MAPK (Erk1/2), phospho-Akt (Ser473), and Akt (pan) (C67E7), all purchased form Cell Signaling Technology. Solutions of primary antibodies were prepared at concentrations recommended by the manufacturer. Membranes were incubated overnight at 4°C with primary antibody solutions. After repeated washing, membranes were incubated with a horseradish peroxidase (HRP)-conjugated secondary antibody for 1 hr, followed by another round of repeated washing. Detection was carried out with an ECL chemiluminescence detection kit (GE Healthcare) using FluorChem E imaging system (ProteinSimple).

Statistical analysis

Pearson's linear correlation coefficient was used to measure the strength of a linear association between effect of dose dependent decrease in volume of spheroids and the corresponding fluorescence intensity viability data (Microsoft Excel). This shape change criterion was used only for intact spheroids that showed volume decrease due to drug treatment.

Results and Discussion

Formation consistency and metabolic activity of ATPS tumor spheroids

One of the key challenges of current 3D cell culture technologies is to conveniently mass produce uniformly-sized spheroids that are individually addressable with drug compounds. Inconsistency of shape and non-uniformity of size of spheroids cause differences in their biological activities due to variations in the distribution of actively proliferating and dormant and necrotic cells within spheroids [16, 23]. This introduces a major difficulty in drug screening applications that often use metabolic activity-based assays such as Alamarblue and MTT for endpoint cell viability quantification. Significant variations

in baseline metabolic activities of cells in different spheroids due to their size/shape differences complicate the interpretation of drug effects on cellular viability [16]. Therefore, producing uniformly shaped and sized spheroids that show a similar baseline metabolic activity is essential for toxicity tests using such assays. Existing spheroid culture techniques such as spinner flask and rotary vessel generate a large number of non-uniform spheroids [24]. Although the hanging drop array approach results in consistent spheroids, culturing, handling, and drug treating of spheroids are cumbersome and require specialized plates that are incompatible with standard plate readers, necessitating transfer of spheroids to standard plates for downstream analysis of drug responses of cells [25,26].

Using the robotic ATPS microtechnology, we demonstrate the capability to mass produce consistently-sized spheroids of three different cancer cells in ultra-low attachment 384-well plates. This approach generates a single spheroid in each well within 24 hrs for MDA-MB-157 and HT-29 cells and 48 hrs for U-87 MG cells. Figure 2a-c shows the histogram of diameter of HT-29, U-87 MG, and MDA-MB-157 spheroids measured 72 hrs post-printing with a density of 1.5×10^4 cells. Spheroids of these three cells show a diameter of 420±24 μm, 390±39 μm and 294±6 μm, respectively. Diameter of spheroids of all three cells within each plate follows a Gaussian distribution. The minimal variations in diameter of spheroids demonstrate the reliability of this protocol for use in screening applications. Next, we show that size of spheroids directly correlates with their baseline metabolic activity levels. With all three cancer cells, a strong linear correlation between volume of growing spheroids and the fluorescence signal resulting from metabolizing of PrestoBlue is observed (Figure 2d-f). This emphasizes the importance of producing uniformly-sized spheroids for studies that utilize metabolic assays to measure changes in cell viability and distinguishing effects of different treatments. We note that during long-term culture of spheroids, development of protrusions or budding from periphery of some spheroids may infrequently happen, causing irregularities in shape and introducing variations in their metabolic activity from round spheroids. Therefore, morphological examination of spheroids may provide additional information that cannot be readily captured with biochemical assays. Finally, we performed confocal microscopy to reconstruct the 3D architecture of spheroids made with the ATPS technology (Figure S1 and Video S1).

Growth and matrix deposition of ATPS spheroids

We imaged spheroids daily to determine changes in their size (Figure 2g-i). With a density of 1.5×10^4 cells, HT-29 cells produced the largest spheroids of 0.038 ± 0.0017 mm^3 at the beginning of the experiment. With the same cell density, U-87 MG and MDA-MB-157 spheroids were 0.031 ± 0.0023 mm^3 and 0.013 ± 0.0003 mm^3 on average, respectively. Analysis of growth curve by curve fitting showed that during the first week of culture spheroid showed rapid growth that slowed subsequently. The rapid growth phase was approximately exponential for all three systems. Within the culture period, HT-29 spheroids showed the largest growth and increased in size to 0.16 ± 0.0022 mm^3 that corresponds to a 321% increase in volume. This was followed by U-87 MG and MDA-MB-157 spheroids with 0.124 ± 0.0025 mm^3 and 0.016 ± 0.0003 mm^3, corresponding to 300% and 23% volume increase, respectively. Therefore, spheroids of different cancer cells generated with the ATPS technology showed normal growth kinetics over time. Slower growth of MDA-MB-157 spheroids could potentially be due to longer cell cycle and

compactness of these cells in 3D culture that limits availability of nutrients and oxygen to cells beyond the peripheral zone of spheroids. We further ensured growth of MDA-MB-157 spheroids through measurements of metabolic activity of cellular spheroids (Figure S2).

Next, we confirmed proliferative status of cells through histological staining of spheroids for the cell proliferation marker Ki-67. Spheroids of all three cell lines showed positive staining of the Ki-67 protein (Figure 3a), validating the morphological measurements above. HT-29 colon cancer spheroids contained substantially larger number of Ki-67$^+$ cells than spheroids of brains and breast cancer cells. This is consistent with the morphological measurements above that showed greater proliferation of HT-29 spheroids. Ki-67$^+$ cells were distributed more toward the periphery of spheroids (in particular for HT-29 spheroids), indicating that these cells consume most of nutrients and oxygen available in the media. Additionally, we immunostained cryosections of spheroids of all three cells for major extracellular matrix (ECM) proteins type I collagen, laminin, and fibronectin (Figure 3b-d). Positive staining indicates that cells in the spheroids deposit the matrix proteins during culture and that collagen I and laminin are more abundant than fibronectin. Again, this is consistent with the growth of ATPS tumor spheroids based on both morphological and histological examinations. Considering that cell-matrix signaling is a major regulator of various functions of cancer cells including cell proliferation [27–29], spheroids provide a model to study targeting of ECM in a tumor microenvironment [13,30].

Quantitative analysis of drug responses of tumor spheroids

Downstream analysis of cellular responses to therapeutics in high throughput screening applications requires an easy-to-use assay to quickly and reliably resolve viability of drug-treated cells. We used a PrestoBlue assay to determine the level of metabolic activity of cells as an indirect measure of cell viability. This assay only involves a single step of reagent addition to wells and subsequently measuring the fluorescence or absorbance signal that correlates with the number of viable cells. We have previously optimized the PrestoBlue assay for use with spheroid cultures to facilitate post-drug screening analysis of cell viability [21,31].

We screened a collection of 25 anticancer compounds against tumor spheroids of HT-29, U-87 MG, and MDA-MB-157 cells. These compounds were selected to include standard chemotherapy drugs used clinically and specific molecular inhibitors to target mutations in these cells (Table S1). Pathophysiology of these cancers involves dysregulated activities of multiple kinase pathways; as such, we included several kinase inhibitors in our collection (Table 1) to evaluate the effect of targeting of kinase pathways on cancer cells residing in tumor spheroids. All tests were done dose-dependently using six drug concentrations and 14 replicates for each concentration, followed by quantification of cellular responses using the PrestoBlue assay. This comprehensive screening generated 75 dose-response graphs similar to that shown in Figure 4 for HT-29 spheroids treated with selumetinib. From each dose-response graph, we computed IC_{50} and E_{max} values that are classical measures of potency and efficacy of a drug (Figure 4), respectively. Generally, a low IC_{50} value is desirable as it indicates that the drug is effective at low concentrations. For anticancer compounds, E_{max} (normalized by 100%) varies between 1 and 0, corresponding to no drug effect and death of all the cells, respectively.

Figure 5 shows results for spheroids of all three cancer cell lines. The top row of the figure lists the drugs. Figure 5a-c shows the values of E_{max} and log (IC_{50}) for HT-29, U-87 MG, and MDA-MB-157 spheroids, respectively. Close examination of Figure 5a shows that there are several drugs that generate very small E_{max} values of smaller than 0.1, i.e. larger than 90% cell death. These include staurosporine, ponatinib, 17-AAG, YM155, and panobinostat. Nevertheless, the corresponding IC_{50} values vary significantly between 0.06 μM for staurosporine to 4.42 μM for ponatinib. Out of five standard chemotherapeutics, cisplatin resulted in the smallest E_{max} of 0.26 and an IC_{50} value of 63 μM, whereas paclitaxel compromised the viability of 54% of cells and showed the smallest IC_{50} of 0.032 μM. Among all 25 compounds, the MEK1/2 inhibitor trametinib produced the smallest IC_{50} of 0.0015 μM and an E_{max} of 0.21. The other two MEK inhibitors, PD0325901 and selumetinib, also gave very low IC_{50} values of 0.089 μM and 0.081 μM with moderate E_{max} values of 0.32 and 0.36, respectively. Responsiveness of HT-29 spheroids to MEK inhibitors is consistent with presence of B-Raf mutations (Table S1) in these cells and demonstrates that ATPS tumor spheroids can reliably predict treatment responses to targeted therapeutic agents [32,33].

With U-87 MG spheroids, five compounds generated E_{max} values of smaller than 0.2: pictilisib, staurosporine, YM155, panobinostat, and crizotinib. The corresponding IC_{50} values ranged from 0.120 μM for YM155 to 6.280 μM for pictilisib. Considering the activitation of the PI-3K pathway in U-87 MG cells (Table S1) [34–36], except for pictilisib, the remaining pathway-specific inhibitors only showed moderate effects on cell viability. Among the chemotherapy drugs, doxorubicin was the most potent with an IC_{50} of 0.236 μM and produced a maximum cell death of 71%. The MDA-MB-157 TNBC spheroids were least responsive to the tested compounds. Only cisplatin and YM155 dropped cell viability below 10%; the IC_{50} values of these two compounds were 19.847 and 3.761 μM, respectively. Although tirapazamine resulted in E_{max} of 0.18, an IC_{50} could not be obtained due to non-sigmoidal dose-response curve that showed a high cell viability except for the largest drug concentration. Interestingly and despite mutations in the TP53 gene (Table S1) that drive oncogenic activation of PI-3K and MAPK pathways in MDA-MB-157 cells [37–39], these spheroids were highly resistant to specific inhibitors of these pathway and maintained high cell viability of 79-100%. In addition, MDA-MB-157 spheroids were completely resistant to paclitaxel, 5-fluorouracil, and oxaliplatin despite responding well to the drugs when cultured as a monolayer [21]. Close cell-cell contacts and expression of drug transporters have been suggested to cause resistance in 3D culture of these cells [21,40–42].

Ranking the performance of anticancer compounds

Potency and efficacy are useful measures to evaluate the response of cancer cell spheroids to a compound. Nevertheless, comparing the performance of different agents against spheroids of the same cancer cells based on these two metrics is difficult. For example, a particular compound may result in a large cell death at high concentrations, whereas a second compound may be moderately toxic to cancer cells at very low concentrations. This issue is clear from screening results in Figure 5. To overcome this problem, we computed the area under the dose-response curve (AUC) resulting from each treatment. AUC combines drug potency and efficacy into a single parameter and thus, offers a quantitative metric to compare performance of different drugs used against spheroids of each cancer cell line [43]. AUC for

selumetinib-treated HT-29 spheroids is shown in Figure 4 using dashed lines. All AUC values were normalized to a 0-1 range for ease of comparison. AUC values approaching zero indicate both high potency and efficacy. We used this approach to generate a ranking system in Figure 6 for compounds tested against each of the three cancer cell lines.

With HT-29 spheroids (Figure 6a), the MEK1/2 inhibitor trametinib received an AUC score of 0.31 and ranked first. This result is consistent with presence of a gain-of-function B-Raf mutation and high activity of the Raf/MEK/ERK signaling pathway in HT-29 cells (Table S1) [44–46]. The other two MEK inhibitors PD0325901 and selumetinib were also effective and resulted in AUC scores of 0.6 and 0.63, respectively; however compared to trametinib, they were 20-fold less potent. Greater effect of trametinib is likely due to specificity of targeting both MEK1 and MEK2 compared to PD0325901 and selumetinib [47]. High potency of trametinib against HT-29 spheroids agrees well with a previous study that showed significant suppression of tumor growth in HT-29 xenografts in nude mice [48]. The protein kinase C (PKC) inhibitor staurosporine ranked second with an AUC value of 0.46. Consistent with previous studies [49], our result suggests that PKC activity is highly upregulated in HT-29 cells and that staurosporine effectively reduces the activity of this signaling molecule in HT-29 spheroids. Other kinase inhibitors in this collection had moderate to minimal effects on HT-29 cells. Specific inhibitors of PI3K pathway including dactolisib, pictilisib, GSK1059615, and PI-103 produced AUC values of 0.82-1. Moderate effect of dactolisib is likely due to inhibition of phosphorylation of Akt in HT-29 cells [50], consistent with the PI3KCA mutation that lead to the activation of downstream protein Akt in these cells (Table S1). Large AUC values of >0.95 with the other three PI3K pathway inhibitors suggests low sensitivity of HT-29 cell spheroids to PI3K-targeting drugs. Survivin suppressant YM-155, heat shock protein 90 inhibitor 17-AAG, and histone deacetylase (HDAC) inhibitor panobinostat were also very effective against HT-29 spheroids and ranked third, fourth, and seventh. We note that these three compounds resulted in greater cell death than trametinib, but their higher IC_{50} resulted in larger AUC values and lower ranking than trametinib. This emphasizes the importance of simultaneous consideration of potency and efficacy parameters in screening applications to provide a quantitative comparison of performance of a panel of compounds. Among the five standard chemotherapy drugs used, paclitaxel and doxorubicin were more effective against HT-29 cells (Figure 6a).

The highest ranked compound against U-87 MG spheroids was YM-155 with AUC value of 0.42, followed by the HDAC inhibitor panobinostat that produced AUC value of 0.61 (Figure 6b). U-87 MG spheroids were sensitive to three chemotherapy compounds doxorubicin, paclitaxel, and 5-fluorouracil that generated AUC values of 0.63-0.82, but showed complete resistance to both platinum-based drugs. Moderate effects of staurosporine and KX2-391 were potentially due to CDK2 and CDC2 inhibition-mediated cell cycle arrest and blocking of SRC kinase-induced oncogenic EGFR signaling in glioblastoma, respectively [51,52]. Despite PTEN mutation and activation of PI3K/Akt signaling pathway in U-87 MG cells (Table S1), the PI3K inhibitors only showed minimal toxicity. With an AUC of 0.83, pictilisib ranked highest among the four PI3K inhibitors used. Among the MEK inhibitors, trametinib was slightly effective against U-87 MG, suggesting that the MAPK/ERK pathway may be active in these cells [53]. Large AUC values with other compounds indicate minimal or lack of toxicity to U-87 MG spheroids.

MDA-MB-157 spheroids were not responsive to majority of tested compounds; only three compounds showed moderate effects against these cells. Doxorubicin, YM155, and ponatinib ranked highest with AUC values of 0.62, 0.73, and 0.75, respectively. It has been shown that P53 mutation in breast cancer cells significantly increases expression of survivin that leads to cells survival and resistance to therapy [54]. Sensitivity of MDA-MB-157 spheroid to YM155, a survivin suppressant, suggests that the p53 mutation in this cell line (Table S1) may be indirectly targeted in breast cancer cells using YM155. H-R produced minimal toxicity possibly due to expression of hyaluronan receptor CD44 on MDA-MB-157 cells that improves the uptake of resveratrol [55]. Remaining compounds were ineffective and generated AUC values of greater than 0.91. Both structural and biological properties of MDA-MB-157 spheroids may contribute to their drug resistance. Unlike HT-29 and U-87 MG cells, these breast cancer cells form densely packed spheroids. These cells are also known to express drug efflux pumps to avoid drug-induced toxicity [40]. In addition, loss of tumor suppressor protein p16 in these cells is associated with stem cell characteristics that drive therapeutic resistance [56].

Overall, the use of AUC parameter enabled quantitative comparison of performance of different drugs against spheroids of cancer cells. This approach allowed identifying compounds such as YM155 and doxorubicin that were effective against spheroids of all three cancer cell lines, suggesting them as useful agents against different cancers. Additionally, it identified compounds such as tirapazamine that resulted in large AUC values for all three cancer cell spheroids, suggesting that this hypoxia-activated compound is not effective against spheroids that mimic early stage tumors and lack hypoxia.

Morphological changes of spheroids in response to treatment

We captured daily images of spheroids to monitor their morphological changes due to treatment with effective compounds. Our observations revealed two types of effects: growth retardation and disintegration. MEK inhibitors trametinib, selumetinib, and PD0325901 blocked growth of B-Raf mutated HT-29 spheroids in nanomolar-range concentrations (Figure 7a-c). The FDA approved drug trametinib effectively inhibited growth of spheroids starting at a 10 nM concentration (Figure 7d). The other two MEK inhibitors showed a similar effect at and above 100 nM (Figure 7d). The PI3K pathway-targeting compounds dactolisib, GSK1059615, and PI-103 inhibited growth of PTEN mutated U-87 MG spheroids at low micromolar concentrations (Figure 7e-h). We observed a strong positive correlation between growth inhibition of spheroids based on morphological characterization and cell viability measurements using metabolic activity data (Table S2). This is consistent with the linear relationship between volume of non-treated spheroids and their viability data (Figure 2g,h). Therefore, morphological measurements may be used as an additional metric to evaluate effectiveness of compounds against tumor spheroids and select concentrations that block growth of spheroids. We note that 17-AAG, ponatinib, staurosporine, and 5- fluorouracil also displayed growth inhibition effects against HT-29 and U-87 MG spheroids. Using high concentrations of these four compounds and MEK and PI3K inhibitors led to disintegration of spheroids. Due to minimal morphological changes of MDA-MB-157 spheroids, they were excluded from this analysis.

Morphological changes of spheroids treated with standard chemotherapy drugs was cell type dependent. The response of U-87 MG spheroids to chemotherapeutics was similar to molecular

inhibitors in terms of growth inhibition at lower drug concentrations and disintegration when larger concentrations were used, whereas HT-29 and MDA-MB-157 spheroids were disintegrated at all effective concentrations (Figure 8). Spheroids of MDA-MB-157 cells showed complete resistance to chemotherapy drugs paclitaxel, 5-fluorouracil, and oxaliplatin. This response could not be captured with monolayer culture of cells; when treated with paclitaxel, monolayer of these cells produced an IC_{50} value of 8 nM [21]. Resistance to standard chemotherapeutics including taxanes is a major hurdle against treating triple negative breast cancers [40,57,58]. Our data underline the importance of implementing relevant tumor models in drug research and discovery to elicit realistic responses from cells.

Molecular targeting of pathway inhibitors

Next, we conducted a target validation study to confirm that growth inhibition of tumor spheroids by MEK and PI3K inhibitors are indeed due to on-target effects. This was an important step to establish that ATPS spheroids could reliably be used to determine mechanisms of action of different drugs. Our analysis of compound screening with HT-29 spheroids ranked trametinib as the most effective MEK inhibitor that significantly blocked growth of spheroids. HT-29 cells have constitutive B-Raf mutation and deregulated activity of the Raf/MEK/ERK pathway (Table S1) [32,33]. To evaluate whether trametinib-mediated growth inhibition of HT-29 spheroids was due to blocking of ERK1/2 activity, we determined total and phosphorylated levels of ERK1/2 by western blotting. Our result showed that HT-29 cells have constitutive ERK phosphorylation that was completely inhibited after 24 and 48 hrs of treatment with trametinib (Figure 9a), indicating a major role for ERK1/2 on regulating growth of HT-29 spheroids.

Among PI3K inhibitors used in this study, pictilisib was the most effective compound against growth of U-87 MG spheroids. PTEN is a major suppressor of the PI3K/Akt pathway [59], and its mutation in U-87 MG cells results in deregulated PI3K/Akt pathway activation and enhanced cell proliferation and survival (Table S1) [35]. Our protein expression analysis confirmed constitutive Akt phosphorylation in U-87 MG spheroids and complete inhibition of phosphorylation after 24 and 48 hrs of treatment with pictilisib (Figure 9b). This validates that growth retardation of U-87 MG spheroids by pictilisib is due, at least in part, to blocking of PI3K/Akt pathway in U-87 MG spheroids. Thus, our protein expression data indicates that tumor spheroids generated with the ATPS microtechnology provide a relevant 3D model to reliably identify intracellular targets of compounds. Additionally, the ability to find drugs that exhibit strong cytostatic effects at low concentrations against growth of cancer cells may offer new opportunities for treating patients along with a cytotoxic drug.

Conclusions

The polymeric aqueous two-phase system (ATPS) microtechnology enables robotic mass-production of uniformly-sized tumor spheroids in standard 384-microwell plates. Resulting spheroids reproduce key features of tumors such as growth and matrix deposition. We demonstrate that an inherent power of this microtechnology is convenient high throughput screening of drug compounds. Dose-dependent screening of a collection of 25 chemical compounds with different targets and mechanisms of action against brain, colon, and breast cancer spheroids combined with a multi-parametric analysis approach identifies compounds that effectively block growth of spheroids of particular cancer cells. Additionally,

we show that morphology of spheroids contains useful information, which is not necessarily captured with metabolic activity-based cell viability assays, and provides a secondary tool to evaluate differential effects of various drugs on tumor spheroids. This approach also enables identifying drugs with cytostatic effects for potential use in combination with cytotoxic compounds. Incorporating this user-friendly 3D cancer cell culture microtechnology into drug discovery pipeline in pharmaceutical industries and core research centers will help bridge a major gap between currently-used monolayer cell cultures with known limitations and expensive animal models for screening anticancer drugs, reduce the number of animal tests by eliminating ineffective compounds from further consideration, and dramatically reduce costs and increase efficiency.

Acknowledgement

The work is supported by grants from National Institutes of Health (R21CA182333) and Ohio Third Frontier (TECG20140954).

Supporting Information (SI)

Actionable mutations in cell lines, Pearson's correlation coefficient between dose dependent decrease in viability of spheroids and growth inhibition by different molecular inhibitors, confocal reconstruction of spheroids generated with the ATPS technology, and metabolic activity measurements of MDA-MB-157 spheroids are shown.

References

1. Eagle, H.; Foley, G. E. Cytotoxicity in human cell cultures as a primary screen for the detection of anti-tumor agents. *Cancer Res*. 1958;18(9):1017-1025.

2. Smalley, K.S.M.; Lioni, M.; Herlyn, M. Life isn't flat: taking cancer biology to the next dimension. *In Vitro Cell Dev Biol Anim*. 2006; 42(8-9):242-247.

3. Waring, M.J.; Arrowsmith, J.; Leach, A.R.; Leeson, P.D.; Mandrell, S.; Owen, R.M.; Pairaudeau, G.; Pennie, W.D.; Pickett, S.D.; Wang, J.; Wallace, O.; Weir, A. An analysis of the attrition of drug candidates from four major pharmaceutical companies. *Nat Rev Drug Discov*. 2015;14(7):475-486.

4. Zambrowicz, B.P.; Sands, A.T. Knockouts model the 100 best-selling drugs--will they model the next 100? *Nat Rev Drug Discov*. 2003;2(1):38-51.

5. Hutchinson,L.; Kirk, R. High drug attrition rates--where are we going wrong? *Nat Rev Clin Oncol*. 2011;8(4):189-190.

6. Hait, W.N. Anticancer drug development: the grand challenges. *Nat Rev Drug Discov*. 2010;9(4):253-254.

7. Pampaloni,F.; Reynaud, E.G.; Stelzer, E.H.K. The third dimension bridges the gap between cell culture and live tissue. *Nat Rev Mol Cell Biol*. 2007;8(10):839-845.

8. Park ,M.H.; Song, B.; Hong, S.; Kim, S.H.; Lee, K. Biomimetic 3D clusters using human adipose derived mesenchymal stem cells and breast cancer cells: A study on migration and invasion of breast cancer cells. *Mol Pharm*. 2016; 7;13(7):2204-13.

9. Tunggal, J.K.; Cowan, D.S.; Shaikh, H.; Tannock, I.F. Penetration of anticancer drugs through solid tissue: a factor that limits the effectiveness of chemotherapy for solid tumors. *Clin Cancer Res*. 1999;5(6):1583-1586.

10. Xu, X.; Farach-Carson, M.C.; Jia, X. Three-dimensional in vitro tumor models for cancer research and drug evaluation. *Biotechnol Adv*. 2014;32(7):1256-1268.

11. Lee, S-H.; Hong, J.H.; Park, H.K.; Park, J.S.; Kim, B.K.; Lee, J.Y.; Jeong, J.Y.; Yoon, G.S.; Inoue, M.; Choi, G.S.; Lee, I.K. Colorectal cancer-derived tumor spheroids retain the characteristics of original tumors. *Cancer Lett*. 2015;367(1):34-42.

12. Eetezadi, S.; De Souza, R.; Vythilingam, M.; Lessa Cataldi, R.; Allen, C. Effects of doxorubicin delivery systems and mild hyperthermia on tissue penetration in 3D cell culture models of ovarian cancer residual disease. *Mol Pharm*. 2015;12(11):3973-3985.

13. Flach, E.H.; Rebecca, V.W.; Herlyn, M.; Smalley, K.S.M.; Anderson, A.R.A. Fibroblasts contribute to melanoma tumor growth and drug resistance. *Mol Pharm*. 2011;8(6):2039-2049.

14. Kenny, P.A.; Lee, G.Y.; Myers, C.A.; Neve, R.M.; Semeiks, J.R.; Spellman, P.T.; Lorenz, K.; Lee, E.H.; Barcellos-Hoff, M.H.; Petersen, O.W.; Gray, J.W.; Bissell, M.J. The morphologies of breast cancer cell lines in three-dimensional assays correlate with their profiles of gene expression. *Mol Oncol*. 2007;1(1):84-96.

15. Fong, E.L.S.; Martinez, M.; Yang, J.; Mikos, A.G.; Navone, N.M.; Harrington, D.A.; Farach-Carson, M.C. Hydrogel-based 3D model of patient-derived prostate xenograft tumors suitable for drug screening. *Mol Pharm*. 2014;11(7):2040-2050.

16. Ham, S.L.; Joshi, R.; Thakuri, P.S.; Tavana, H. Liquid-based three-dimensional tumor models for cancer research and drug discovery. *Exp Biol Med*. 2016;241(9):939-54

17. Tavana, H.; Jovic, A.; Mosadegh, B.; Lee, Q.Y.; Liu, X.; Luker, K.E.; Luker, G.D.; Weiss S.J.; Takayama, S. Nanolitre liquid patterning in aqueous environments for spatially defined reagent delivery to mammalian cells. *Nat Mater*. 2009;8(9):736-741.

18. Ham, S.L.; Atefi, E.; Fyffe, D.; Tavana, H. Robotic production of cancer cell spheroids with an aqueous two-phase system for drug testing. *J Vis Exp*. 2015;(98).

19. Atefi, E.; Joshi, R.; Mann, J.A.; Tavana, H. Interfacial tension effect on cell partition in aqueous two-phase systems. *ACS Appl Mater Interfaces*. 2015;7(38):21305-21314.

20. Atefi, E.; Mann, J.A.; Tavana, H. Ultralow interfacial tensions of aqueous two-phase systems measured using drop shape. *Langmuir*. 2014;30(32):9691-9699.

21. Lemmo, S.; Atefi, E.; Luker, G.D.; Tavana, H. Optimization of aqueous biphasic tumor spheroid microtechnology for anti-cancer drug testing in 3D culture. *Cell Mol Bioeng*. 2014;7(3):344-354.

22. Da Violante, G.; Zerrouk, N.; Richard, I.; Provot, G.; Chaumeil, J.C.; Arnaud, P. Evaluation of the cytotoxicity effect of dimethyl sulfoxide (DMSO) on Caco2/TC7 colon tumor cell cultures. *Biol Pharm Bull*. 2002;25(12):1600-1603.

23. Walenta, S.; Doetsch, J.; Mueller-Klieser, W.; Kunz-Schughart, L. A. Metabolic imaging in multicellular spheroids of oncogene-transfected fibroblasts. *J Histochem Cytochem*. 2000;48(4):509-522.

24. Ingram, M.; Techy, G.B.; Saroufeem, R.; Yazan, O.; Narayan, K.S.; Goodwin, T.J.; Spaulding, G.F. Three-dimensional growth patterns of various human tumor cell lines in simulated microgravity of a NASA bioreactor. *In Vitro Cell Dev Biol Anim*. 1997;33(6):459-466.

25. Kelm, J.M.; Timmins, N.E.; Brown, C.J.; Fussenegger, M.; Nielsen, L.K. Method for generation of homogeneous multicellular tumor spheroids applicable to a wide variety of cell types. *Biotechnol Bioeng*. 2003;83(2):173-180.

26. Hsiao, A.Y.; Tung, Y-C.; Kuo, C-H.; Mosadegh, B.; Bedenis, R.; Pienta, K.J.; Takayama, S. Micro-ring structures stabilize microdroplets to enable long term spheroid culture in 384 hanging drop array plates. *Biomed Microdevices*. 2012;14(2):313-323.

27. Lee, K.; Nam, K.; Oh, S.; Lim, J.; Kim, Y.P.; Lee, J.W.; Yu, J.H.; Ahn, S.H.; Kim, S.B.; Noh, D.Y.; Lee, T.; Shin, I. Extracellular matrix protein 1 regulates cell proliferation and trastuzumab resistance through activation of epidermal growth factor signaling. *Breast Cancer Res*. 2014;16(6):479.

28. Gérard, C.; Goldbeter, A. The balance between cell cycle arrest and cell proliferation: control by the extracellular matrix and by contact inhibition. *Interface Focus*. 2014;4(3):20130075.

29. Ulrich, T.A.; de Juan Pardo, E.M.; Kumar, S. The mechanical rigidity of the extracellular matrix regulates the structure, motility, and proliferation of glioma cells. *Cancer Res*. 2009;69(10):4167-4174.

30. Venning, F.A.; Wullkopf, L.; Erler, J.T. Targeting ECM Disrupts Cancer Progression. *Front Oncol*. 2015;5:224.

31. Atefi,E.; Lemmo, S.; Fyffe, D.; Luker, G.D.; Tavana, H. High throughput, polymeric aqueous two-phase printing of tumor spheroids. *Adv Funct Mater*. 2014;24(41):6509-6515.

32. Fang, J.Y.; Richardson, B.C. The MAPK signalling pathways and colorectal cancer. *Lancet Oncol*. 2005;6(5):322-327.

33. Yeh, J.J.; Routh, E.D.; Rubinas, T.; Peacock, J.; Martin, T.D.; Shen, X.J.; Sandler, R.S.; Kim, H.J.; Keku, T.O.; Der, C.J. KRAS/BRAF mutation status and ERK1/2 activation as biomarkers for MEK1/2 inhibitor therapy in colorectal cancer. *Mol Cancer Ther*. 2009;8(4):834-843.

34. Knobbe, C.B.; Merlo, A.; Reifenberger, G. Pten signaling in gliomas. *Neuro Oncol*. 2002;4(3):196-211.

35. Klingler-Hoffmann, M.; Bukczynska, P.; Tiganis, T. Inhibition of phosphatidylinositol 3-kinase signaling negates the growth advantage imparted by a mutant epidermal growth factor receptor on human glioblastoma cells. *Int J cancer*. 2003;105(3):331-339.

36. Clark, M.J.; Homer, N.; O'Connor, B.D.; Chen, Z.; Eskin, A.; Lee, H.; Merriman, B.; Nelson, S.F. U87MG decoded: the genomic sequence of a cytogenetically aberrant human cancer cell line. *PLoS Genet*. 2010;6(1):e100083.

37. Lawrence, R.T.; Perez, E.M.; Hernández, D.; Chris, P. M.; Miller ,C.P.; Haas, K.M.; Irie, H. Y.; Lee, Su-In.; Blau, C.A.; Villen, J. The proteomic landscape of triple-negative breast cancer. *Cell Rep*. 2015;11(4):630-644.

38. Walerych, D.; Napoli, M.; Collavin, L.; Del Sal, G. The rebel angel: mutant p53 as the driving oncogene in breast cancer. *Carcinogenesis*. 2012;33(11):2007-2017.

39. Yuen, H-F.; Abramczyk, O.; Montgomery, G.; Chan, K.K.; Huang, Y.H.; Sasazuki, T.; Shirasawa, S.; Gopesh, S.; Chan, K.W.; Fennell, D.; Janne, P.; El-Tanani, M.; Murray, J.T. Impact of oncogenic driver mutations on feedback between the PI3K and MEK pathways in cancer cells. *Biosci Rep*. 2012;32(4):413-422.

40. VanKlompenberg, M.K.; Bedalov, C.O.; Soto, K.F.; Prosperi, J.R. APC selectively mediates response to chemotherapeutic agents in breast cancer. *BMC Cancer*. 2015;15(1):457.

41. Olive, P.L.; Durand, R.E. Drug and radiation resistance in spheroids: cell contact and kinetics. *Cancer Metastasis Rev*. 1994;13(2):121-138.

42. Kerbel, R.S.; St Croix, B.; Florenes, V.A.; Rak, J. Induction and reversal of cell adhesion-dependent multicellular drug resistance in solid breast tumors. *Hum Cell*. 1996;9(4):257-264.

43. Fallahi-Sichani, M.; Honarnejad, S.; Heiser, L.M.; Gray, J.W.; Sorger, P.K. Metrics other than potency reveal systematic variation in responses to cancer drugs. *Nat Chem Biol*. 2013;9(11):708-714.

44. Ahmed, D.; Eide, P.W.; Eilertsen, I.A.; Danielsen, S.A.; Eknæs, M.; Hektoen, M.; Lind, G.E.; Lothe, R.A. Epigenetic and genetic features of 24 colon cancer cell lines. *Oncogenesis*. 2013;2:e71.

45. Chow, A.K.M.; Cheng, N.S.M.; Lam, C.S.C; Ng, L.; Wong, S.K.; Wan, T.M.; Man, J.H.; Cheung, A.H.; Yau, T.C.; Poon, J.T.; Law, W.L.; Pang, R.W. Preclinical analysis of the anti-

tumor and anti-metastatic effects of Raf265 on colon cancer cells and CD26(+) cancer stem cells in colorectal carcinoma. *Mol Cancer*. 2015;14:80.

46. Oikonomou, E.; Makrodouli, E.; Evagelidou, M.; Joyce, T.; Probert, L.; Pintzas, A. BRAF(V600E) efficient transformation and induction of microsatellite instability versus KRAS(G12V) induction of senescence markers in human colon cancer cells. *Neoplasia*. 2009;11(11):1116-1131.

47. McDermott, L.; Qin, C. Allosteric MEK1/2 inhibitors for the treatment of cancer: an overview. *J drug Res Dev*. 2015;1(1):1-9.

48. Yamaguchi, T.; Kakefuda, R.; Tajima, N.; Sowa, Y.; Sakai, T. Antitumor activities of JTP-74057 (GSK1120212), a novel MEK1/2 inhibitor, on colorectal cancer cell lines in vitro and in vivo. *Int J Oncol*. 2011;39(1):23-31.

49. Qiao, L.; Koutsos, M.; Tsai, L.L.; Kozoni, V.; Guzman, J.; Shiff, S.J.; Rigas, B. Staurosporine inhibits the proliferation, alters the cell cycle distribution and induces apoptosis in HT-29 human colon adenocarcinoma cells. *Cancer Lett*. 1996;107(1):83-89.

50. Mueller, A.; Bachmann, E.; Linnig, M.; Khillimberger, K.; Schimanski, C.C.; Galle, P.R.; Moehler, M. Selective PI3K inhibition by BKM120 and BEZ235 alone or in combination with chemotherapy in wild-type and mutated human gastrointestinal cancer cell lines. *Cancer Chemother Pharmacol*. 2012;69(6):1601-1615.

51. Harmalkar, M.N.; Shirsat, N. V. Staurosporine-induced growth inhibition of glioma cells is accompanied by altered expression of cyclins, CDKs and CDK inhibitors. *Neurochem Res*. 2006;31(5):685-692.

52. Lu, K. V.; Zhu, S.; Cvrljevic, A.; Huang, T.T.; Sarkaria, S.; Ahkavan, D.; Dang, J.; Dinca, E.B.; Plaisier, S.B.; Oderberg, I.; Lee, Y.; Chen, Z.; Caldwell, J.S.; Xie, Y.; Loo, J.A.; Seligson, D.; Chakravari, A.; Lee, F.Y.; Weinmann, R.; Cloughesy, T.F.; Nelson, S.F.; Bergers, G.; Graeber, T.; Furnari, F.B.; James, C.D.; Cavenee, W.K.; Johns, T.G.; Mischel, P.S. Fyn and SRC are effectors of oncogenic epidermal growth factor receptor signaling in glioblastoma patients. *Cancer Res*. 2009;69(17):6889-6898.

53. Cha, J.H.; Choi, Y.J.; Cha, S.H.; Choi, C.H.; Cho, W.H. Allicin inhibits cell growth and induces apoptosis in U87MG human glioblastoma cells through an ERK-dependent pathway. *Oncol Rep*. 2012;28(1):41-48.

54. Végran, F.; Boidot, R.; Oudin, C.; Defrain, C.; Rebucci, M.; Lizard-Nacol, S. Association of p53 gene alterations with the expression of antiapoptotic survivin splice variants in breast cancer. *Oncogene*. 2007;26(2):290-297.

55. Ham, S,L.; Nasrollahi, S.; Shah, K.N.; Soltisz, A.; Paruchuri, S.; Yun, Y.H.; Luker, G.D.; Bishayee, A.; Tavana, H. Phytochemicals potently inhibit migration of metastatic breast cancer cells. *Integr Biol*. 2015;7(7):792-800.

56. Arima,Y.; Hayashi, N.; Hayashi, H.; Sasaki, M.; Kai, K.; Sugihara, E.; Abe, E.; Yoshida, A.; Mikami, S.; Nakamura, S.; Saya, H. Loss of p16 expression is associated with the stem cell characteristics of surface markers and therapeutic resistance in estrogen receptor-negative breast cancer. *Int J cancer*. 2012;130(11):2568-2579.

57. Akashi-Tanaka, S.; Watanabe, C.; Takamaru, T.; Kuwayama, T.; Ikeda, M.; Ohyama, H.; Mori, M.; Yoshida, R.; Hashimoto, R.; Terumasa, S.; Enokido, K.; Hirota, Y.; Okuyama, H.; Nakamura, S. BRCAness predicts resistance to taxane-containing regimens in triple negative breast cancer during neoadjuvant chemotherapy. *Clin Breast Cancer*. 2015;15(1):80-85.

58. Sprouse, A.A.; Herbert, B-S. Resveratrol augments paclitaxel treatment in MDA-MB-231 and paclitaxel-resistant MDA-MB-231 breast cancer cells. *Anticancer Res*. 2014;34(10):5363-5374.

59. Song, M.S.; Salmena, L.; Pandolfi, P.P. The functions and regulation of the PTEN tumour suppressor. *Nat Rev Mol Cell Biol*. 2012;13(5):283-296.

Table 1. List of anticancer compounds and their main targets

Compound	Target
Paclitaxel	Microtubules
Oxaliplatin	DNA crosslinker
5-Fluorouracil	Thymidylate synthase
Cisplatin	DNA crosslinker
Doxorubicin	Topoisomerase II
Dactolisib	mTOR/PI3K
PI-103	PI3K
Pictilisib	PI3K
GSK1059615	PI3K
PD0325901	MEK1
Selumetinib	MEK1
Trametinib	MEK1/2
SP600125	JNK
Staurosporine	PKC
Ponatinib	TK
VER155008	HSP70
17-AAG	HSP90
YM155	Survivin
Ribociclib	CDK
Panobinostat	HDAC
LY2784544	JAK2
KX2-391	SRC
Crizotinib	C-MET/ALK
H-R	ROS
Tirapazamine	Hypoxia

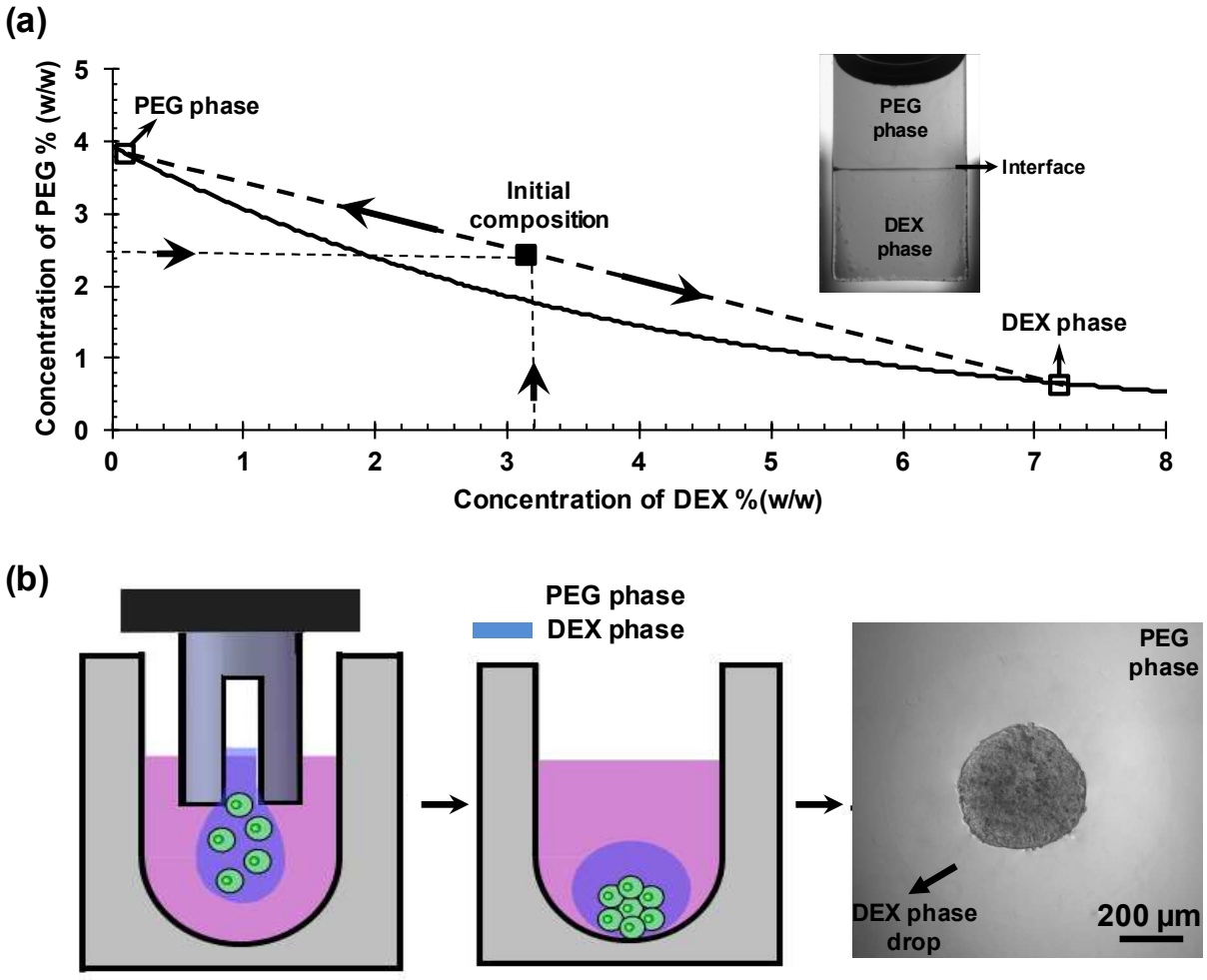

Figure 1: (a) Phase diagram of ATPS made with polyethylene glycol (PEG) and dextran (DEX) shows the composition of the initial two-phase mixture (solid square) and resulting segregated phases (open squares). The inset image shows side view of the ATPS formed in a glass cuvette with the location of the interface indicated. (b) Schematic representation of spheroid generation using the ATPS microtechnology and top view of a spheroid of HT-29 colon cancer cells.

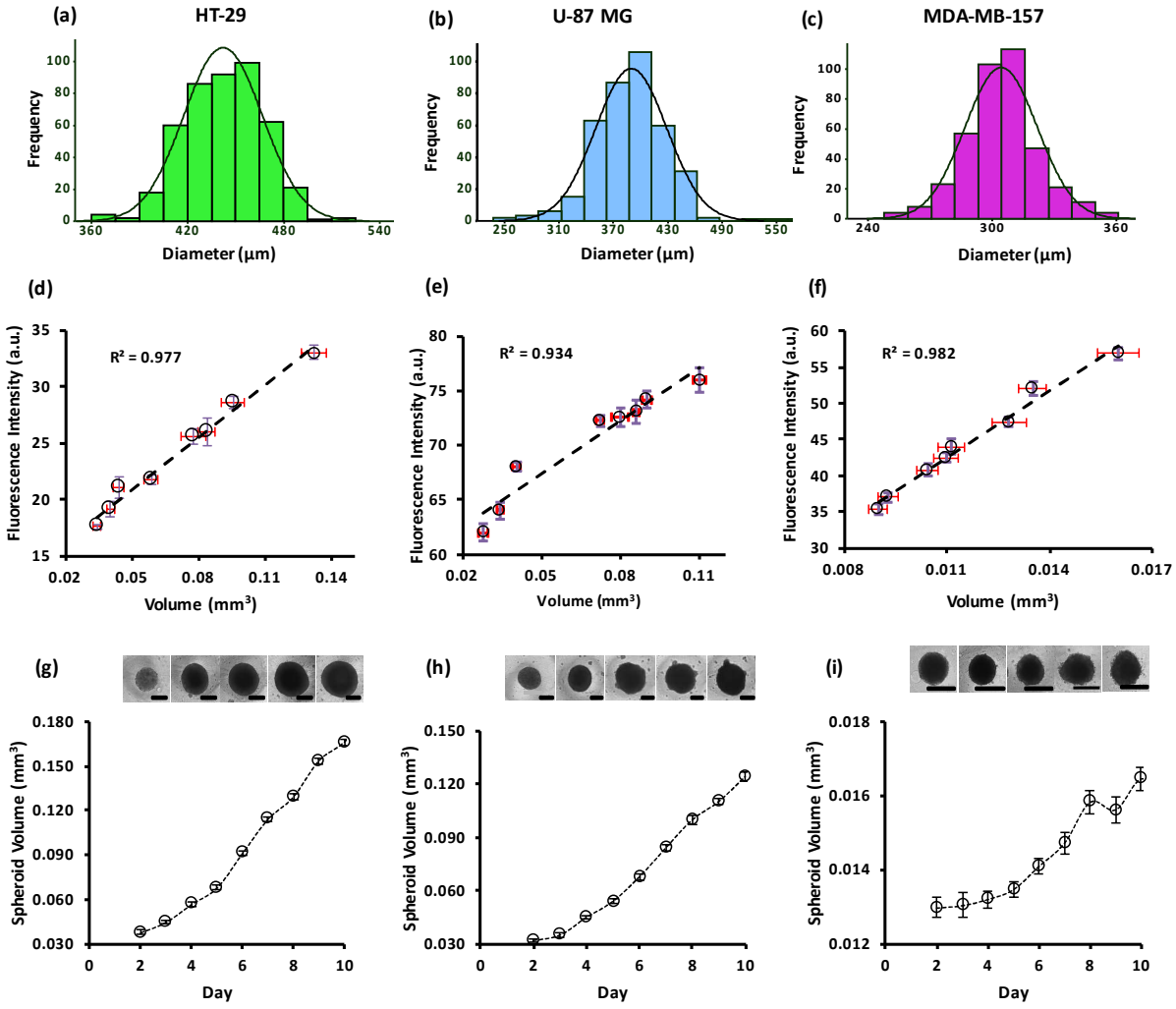

Figure 2: Histogram of diameter of spheroids of (a) HT-29 colon cancer cells, (b) U-87 MG brain cancer cells, and (c) MDA-MB-157 breast cancer cells shows the consistency of size of spheroids (n=300). Fitted curves show that diameter of spheroids follows a Gaussian distribution. (d-f) Metabolic activity of spheroids, measured as the fluorescence signal produced by cells metabolizing PrestoBlue, shows a linear correlation with the size of spheroids. Horizontal and vertical bars represent standard error of volume of spheroids and standard error of raw fluorescence intensity data (n=7 for each data point). (g-i) Volume growth kinetics of HT-29, U-87 MG, and MDA-MB-157 spheroids is shown over time. Images represent spheroids from different days of culture. The number of samples for each time point is 50 spheroids and error bars represent standard error of mean. Scale bar: 300 µm

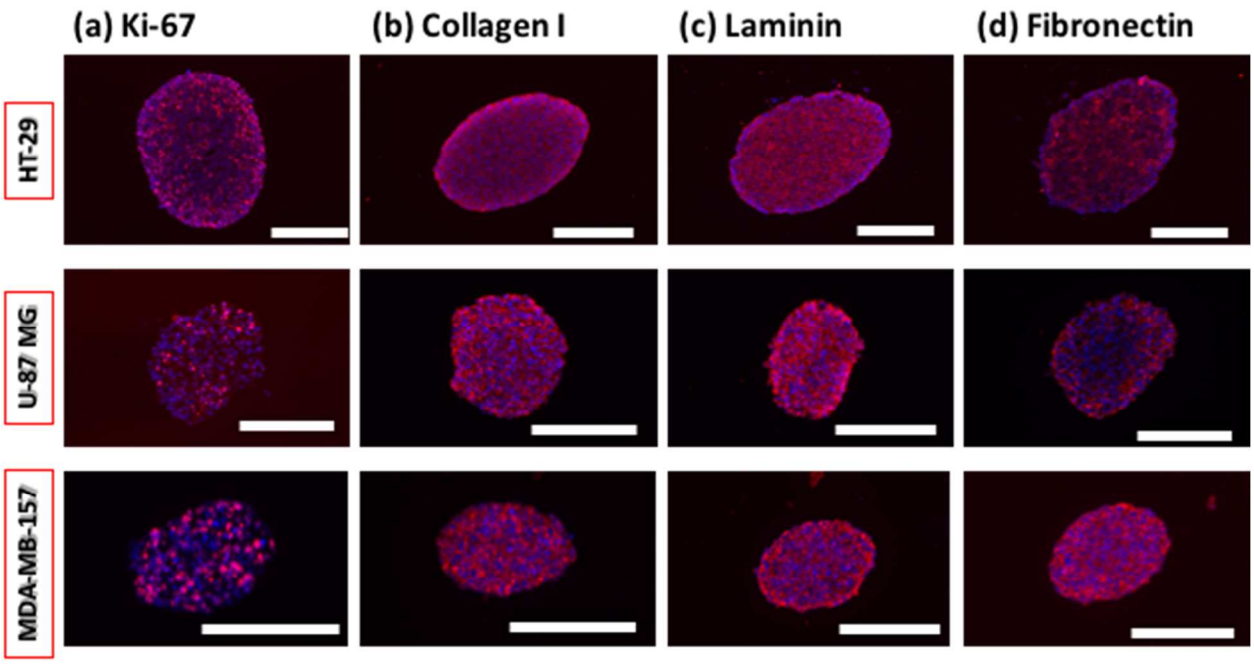

Figure 3: Histological staining of spheroids of HT-29 (top row), U-87 MG (middle row), and MDA-MB-157 (bottom row) cells for (a) Ki-67 cell proliferation marker, (b) type I collagen, (c) laminin, and (d) fibronectin. Blue represents nuclei staining with Hoechst and pink represents protein staining. Scale bar: 200 µm

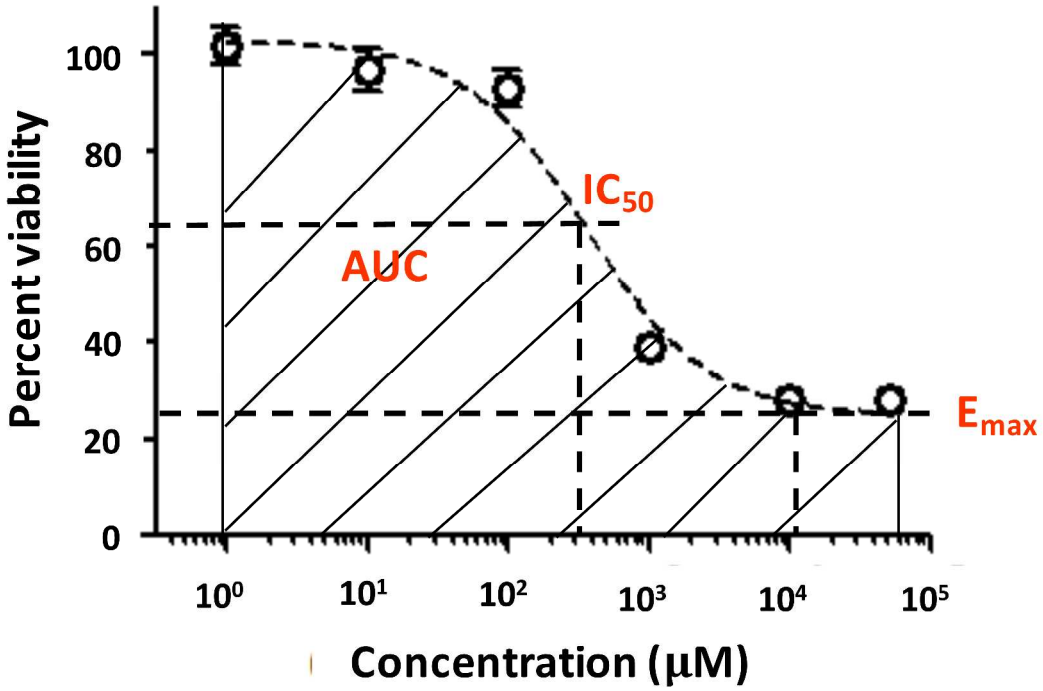

Figure 4: A representative dose-response curve is shown for experiment with selumetinib against HT-29 spheroids. Half-maximum inhibitory concentration (IC_{50}), maximum inhibition (E_{max}), and area under the curve (AUC) are used for multi-parametric analysis of cellular responses to drug compounds.

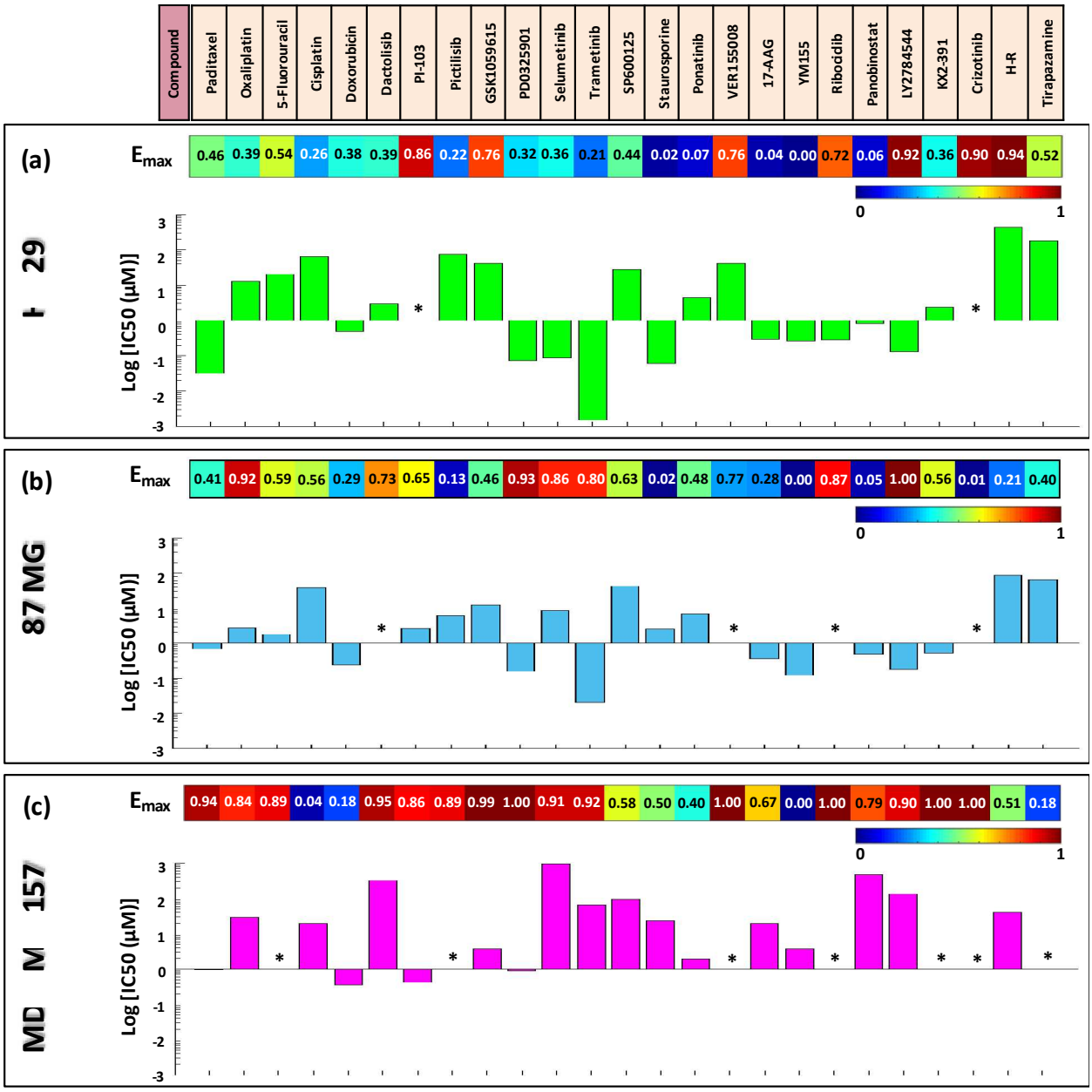

Figure 5: Twenty five Anticancer compounds are listed in the top row. Values of E_{max} and log (IC_{50}) for drug-treated spheroids of (a) HT-29, (b) U-87 MG, and (c) MDA-MB-157 are shown. Color bar indicates the range of E_{max} (0-1). In addition, E_{max} values for tested compounds are shown. * denotes the lack of an IC_{50} value in the dose-response graph of the particular drug-cell pair.

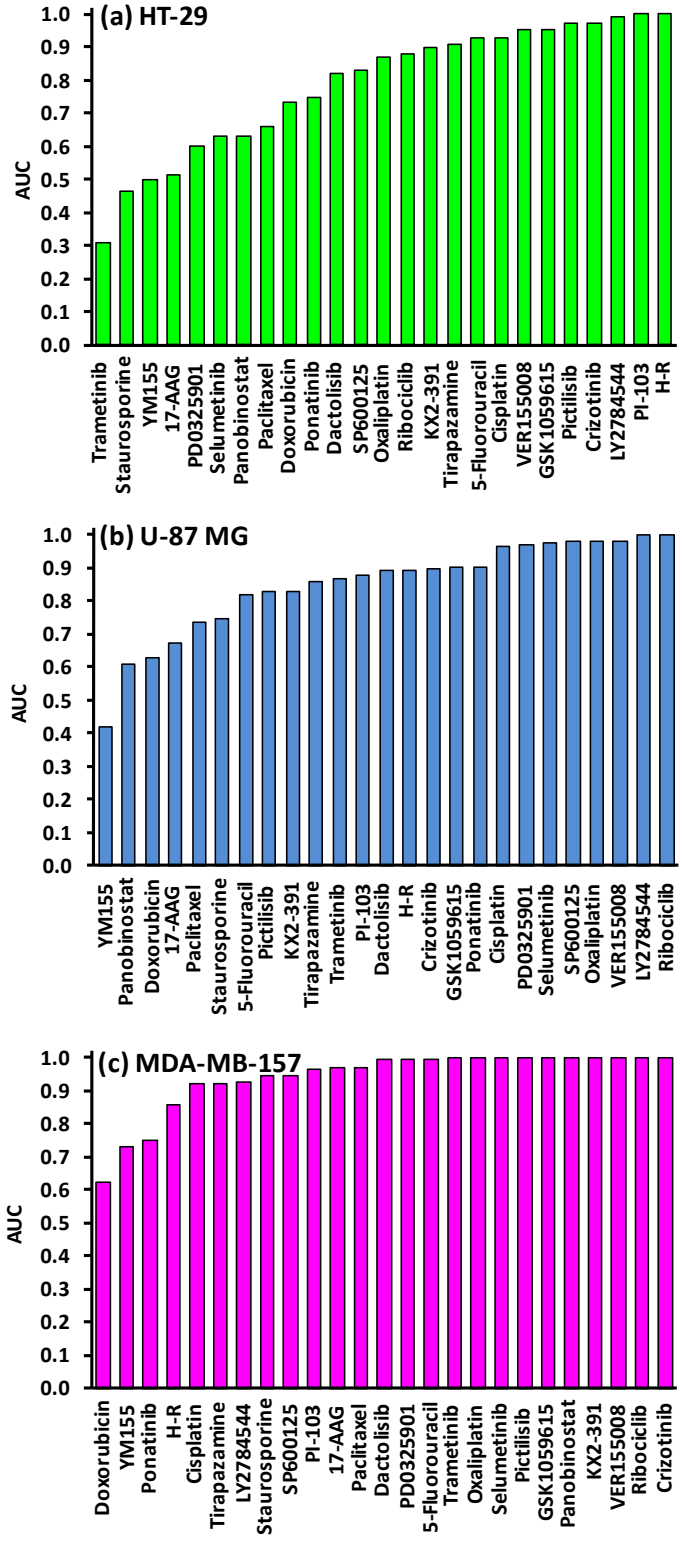

Figure 6: Ranking of effectiveness of compounds based on the AUC metric for spheroids of (a) HT-29, (b) U-87 MG, and (c) MDA-MB-157 cells.

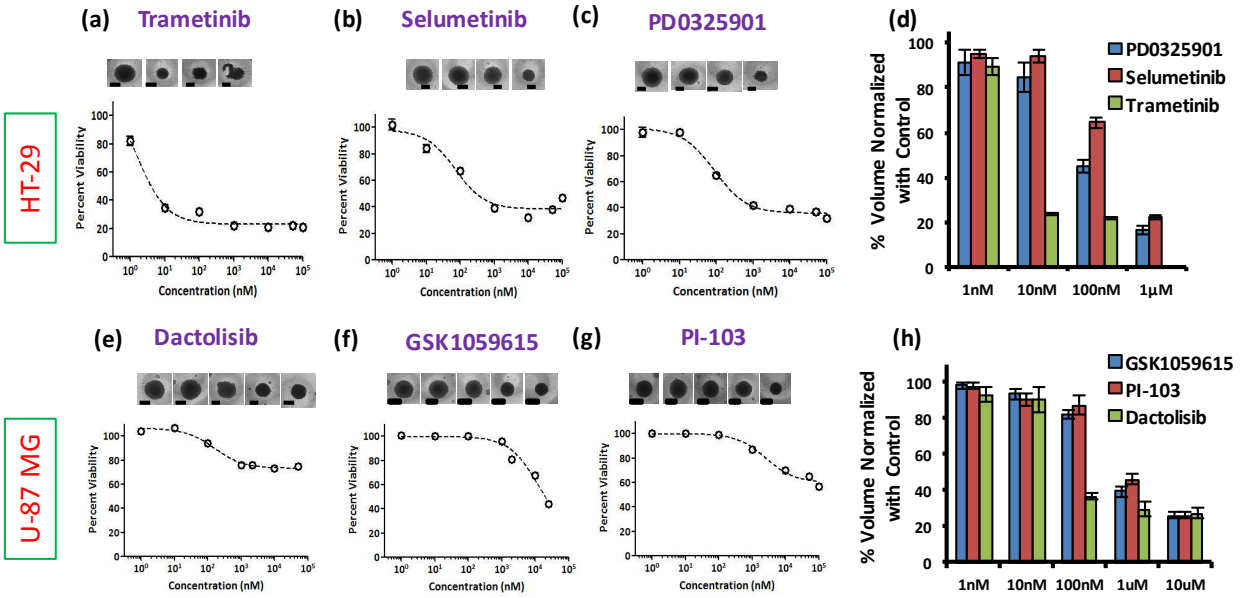

Figure 7: Growth inhibition of spheroids of HT-29 and U-87 MG cells after treatment with specific MEK and PI3K inhibitors. Panels (a-c) show dose-dependent blocking of HT-29 spheroids growth due to treatment with three different MEK inhibitors, consistent with measured viability data with each compound. (d) Comparison of growth inhibition of HT-29 spheroids at different concentrations of MEK inhibitors. Panels (e-g) display dose-dependent growth retardation of U-87 MG spheroids treated with three different PI3K inhibitors. (h) Comparison of growth inhibition of U-87 MG spheroids due to treatment with different PI3K inhibitors. Scale bar: 300 µm

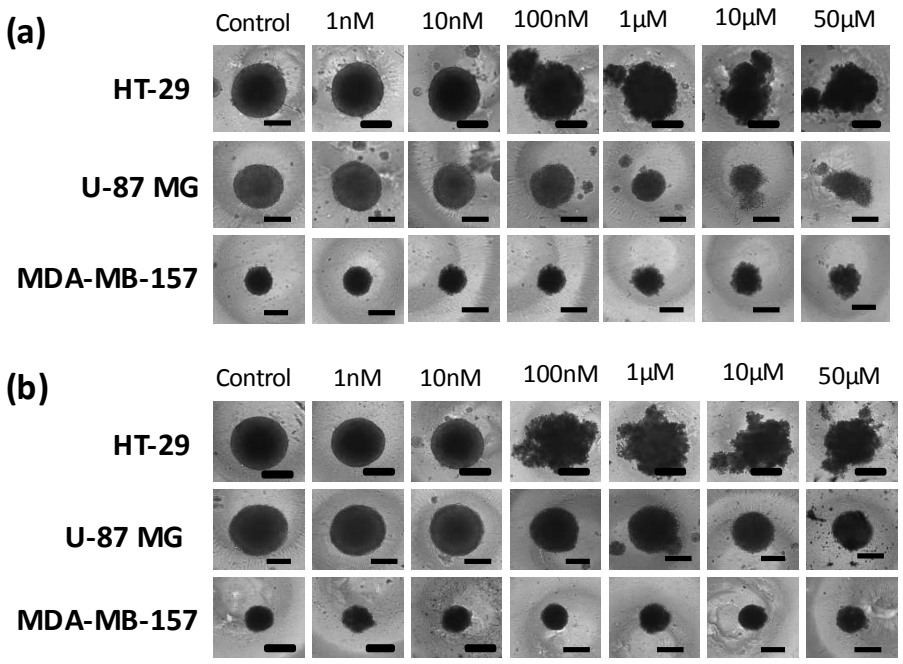

Figure 8: Morphological changes of spheroids of HT-29, U-87 MG, and MDA-MB-157 cells after treatment with (a) doxorubicin and (b) paclitaxel at different concentrations of drugs. Disintegration of HT-29 spheroids is observed with both chemotherapeutics. Growth of U-87 MG spheroids is blocked at sub-micromolar concentrations, whereas higher drug concentrations disintegrate the spheroids. HT-29 and MDA-MB-157 spheroids show disintegration at all effective drug concentrations. MDA-MB-157 spheroids show complete resistance to paclitaxel and minimal morphological changes. Scale bar: 300 µm

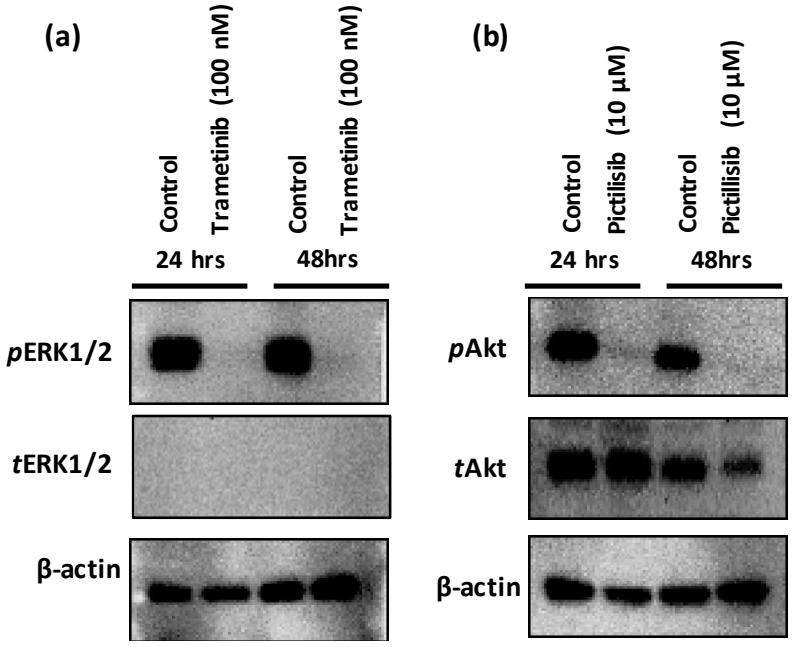

Figure 9: (a) Trametinib inhibition of ERK1/2 phosphorylation in HT-29 spheroids, and (b) pictilisib inhibition of Akt phosphorylation in U-87 MG spheroids are shown at two different time points.